European Journal of Mechanics B/Fluids 28 (2009) 521–531

Contents lists available at ScienceDirect

European Journal of Mechanics B/Fluids

www.elsevier.com/locate/ejmflu

Occurrence of standing surface gravity waves modulation in shallow water

A. Ezersky [a,*], A. Slunyaev [b], D. Mouazé [a], W. Chokchai [a]

[a] UMR CNRS 6143 "Morphodynamique Continentale et Côtière" (M2C), Université de Caen-Basse Normandie, 2-4 rue des Tilleuls, 14000 Caen, France
[b] Institute of Applied Physics, Russian Academy of Sciences, 46 Ulyanov Street GSP-120, 603950 Nizhny Novgorod, Russia

ARTICLE INFO

Article history:
Received 19 November 2008
Received in revised form 3 February 2009
Accepted 3 February 2009
Available online 7 February 2009

Keywords:
Surface gravity waves
Shallow water
Modulation instability

ABSTRACT

Arising of modulations of surface gravity waves in a shallow water resonator under harmonic forcing is investigated in laboratory experiments. Different types of modulations are found, when the wave amplitude exceeds a certain threshold. Bifurcation diagram on the plane "amplitude of excitation – frequency of excitation" is determined. Numerical simulations of the Euler equations within the frameworks of the High-Order Spectral Method are performed with the purpose of reproducing the modulational regimes observed in the laboratory experiments. The simulations allowed us to determine physical mechanisms responsible for the occurrence of modulated waves.

1. Introduction

Regular water waves are known to suffer from different kinds of instabilities. The instabilities spawn a redistribution of wave energy in space and thus lead to the formation of large waves or wave groups. Modulational instability is a classical kind of gravity wave instability, found by Benjamin and Feir in 1967 [1]. In the weakly-nonlinear approximation the modulational instability is usually called after Benjamin and Feir and may be considered within an approximate nonlinear parabolic equation (or the nonlinear Schrödinger, NLS, equation, first derived for water waves in [2]). It is well-known that a harmonic traveling wave of small, but finite, amplitude a can be modulationally unstable if the water depth, h, meets the condition $kh > 1.363$, where k is the wave number; then Lighthill's condition is fulfilled:

$$\omega_0''(k)\omega_2(k) < 0, \tag{1.1}$$

see for instance [3]. In (1.1) $\omega_0(k)$ is the dispersion relation for linear waves, and $\omega_2(k)$ is the nonlinear addition to the frequency, $\omega(k) = \omega_0(k) + \omega_2(k)|ka|^2$. In other words, Lighthill's condition (1.1) means that the negative dispersion of surface gravity waves, $\omega_0''(k) < 0$, is compensated by a positive nonlinear shift of frequency, and due to this compensation the resonance conditions for harmonics interaction become fulfilled. This simple qualitative explanation is valid when waves are close to sinusoidal.

The nonlinear addition to frequency depends on the liquid depth. When the water becomes shallower, $kh < 1.363$, the nonlinear correction to frequency changes its sign, and the Lighthill instability criterion (1.1) is not satisfied. The sign change of nonlinear frequency shift is actually due to the induced current which becomes important in shallow-water conditions and must be taken into account. The induced current modifies the nonlinear term in the NLS equation, and may change its sign. This and other types of instabilities, when weak longitudinal, or skew or transverse perturbations of uniform unidirectional waves are unstable, have been investigated in ample detail theoretically (see for example three-dimensional NLS-like theory in [4,5], and strongly nonlinear study in [6]). It was found in particular that finite depth of a liquid (depth $kh < 1.363$) produces unstable waves only at sufficiently large amplitudes: the less the water depth is, the larger are the amplitudes at which instability arises. Two-dimensional perturbations (in two horizontal directions) are preferable for instability in this case.

It is significant to note that the stability analysis becomes trickier when shallow-water waves are considered; some recent study of shallow-water wave instabilities, including the strongly nonlinear case, may be found in [7]. Modulational instability may occur in the case of cross-wave systems as well; coupled NLS-like equations are usually derived in this case, see [8] and references therein. Two counter propagating waves may be considered as a limiting case of crossed waves, and they represent the case of a standing wave in a resonator. Despite a large number of theoretical works concern modulational instability of propagating waves, it is still unclear when instability of nonlinear standing waves in a liquid of finite depth may occur. In [9] is reported that, weakly nonlinear standing water waves are modulationally unstable only if the component traveling waves are modulation unstable. However, in [10] and also in [11] authors claim that if a wave is modulationally stable in the absence of counter propagating wave, its couple may lead to the existence of the effect of modulational instability.

In this paper we investigate modulations of standing waves of finite amplitude excited in a shallow water resonator by harmonic

* Corresponding author.
E-mail address: Alexander.Ezersky@unicaen.fr (A. Ezersky).

0997-7546/$ – see front matter
doi:10.1016/j.euromechflu.2009.02.001

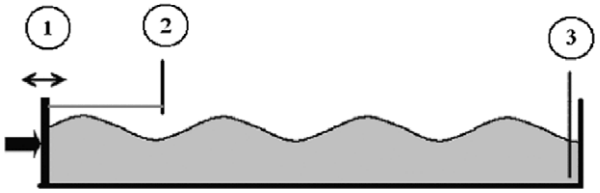

Fig. 1. The scheme of the experiments, (1) is the wavemaker, (2) is the transducer of horizontal displacement of wave maker, (3) is the resistive probe of a free surface displacement.

forcing. The paper deals with the results of laboratory experiments, and their interpretation with the help of strongly-nonlinear simulations. The paper is organized as follows. At the beginning the description of experimental setup (Section 2) and results obtained in the laboratory investigation of modulated waves in a water flume (Section 3) are presented. Later on, in Section 4, we present results on numerical simulation of different regimes of water wave modulation in a flume. In Sections 5 and 6, we investigate the physical mechanism of modulations; and in Section 7, conclusions are formulated.

2. Experimental setup

Tests were carried out in a hydrodynamic channel, see Fig. 1. The length of the channel is $L = 15$ m, its width is $d = 0.5$ m, and the depth of the liquid layer is $h = 0.17$ m. A piston type wavemaker consisting of a vertical plate set in motion by a DC engine was placed at one end of the channel. The plate was moved in the horizontal direction by a harmonic law. The horizontal displacement of the wavemaker was controlled by a special transducer. Our measurements showed us that the levels of harmonics multiple to the frequency of excitation were less than several percent. Amplitude B and oscillation frequency f of the wavemaker could be changed: the amplitude, by changing position of the eccentric connecting the engine and the plate; and the frequency, by changing supply voltage of the engine. The wavemaker motion was controlled by a displacement transducer. Free surface oscillations were registered by resistive wave gage placed at the end of the channel (see Fig. 1). Signals from the surface wave transducers and wavemaker displacement were recorded in a computer simultaneously for further data processing.

The channel used during the tests represents a resonator for surface gravity waves. Natural frequencies of resonator modes, f_n, are defined by the dispersion relation as

$$f_n = \frac{1}{2\pi}\sqrt{g\frac{\pi}{L}n\tanh\left(\frac{\pi}{L}nh\right)}, \quad n = 1, 2, 3, \ldots, \tag{2.1}$$

where n numerates the modes, and g is the gravity acceleration.

The experiment was accomplished at the frequencies $0.34\ \text{Hz} < f < 0.48\ \text{Hz}$ corresponding to the excitation of modes with numbers $8 < n < 12$, hence, in the experiment we have the depth parameter $0.28 < kh < 0.42$.

3. Observation of occurrence of modulations in the laboratory tank

Three regimes were observed in the experiments. They are: (1) steady-state generation of nonlinear waves with constant amplitude; (2) regime with modulation, including chaotic modulation without wave breaking; and (3) regime with modulation accompanied by wave breaking. A map of these regimes on a plane (amplitude of oscillation of the wavemaker plate, B, versus oscillation frequency, f) is given in Fig. 2.

Each point in this diagram was obtained by the following procedure. We begin excitation of waves (switch on the wavemaker)

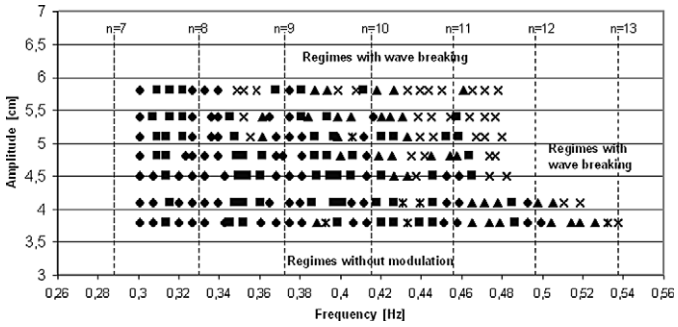

Fig. 2. The diagram of the regimes observed in the laboratory experiments (amplitude of the wavemaker versus its frequency): rhombs correspond to the regimes of generation of constant-amplitude waves; squares – regimes with regular modulated waves; triangles – regimes with chaotic wave modulation; stars show regimes with double modulation, crosses show regimes with wave breaking. The dashed lines correspond to the linear frequencies of the natural modes with the numbers indicated in the figure.

with flat free surface of the liquid; it corresponds to the zero initial conditions. We wait for approximately 10 minutes to avoid transitional regime and after that we record time series of the free surface displacement.

It is clear from the diagram that the wave modulation and breaking arise at smaller amplitudes of wavemaker oscillations if the excitation frequency does not coincide with the natural frequency of resonator modes (2.1).

Time series of the free surface displacement obtained at different regimes in the flume are presented in Fig. 3. An excitation of harmonics with frequencies multiple to the frequency of external forcing occurs for the regime without modulation. Consequently, a nonlinear steady wave is recorded (see Fig. 3(a)). For the regime with regular modulation the smallest period of the envelope wave (see Fig. 3(b)) was approximately equal to the period of basic mode of resonator: $T_1 = 1/f_1$, where $f_1 \approx 0.04$ Hz.

It was revealed that periods of the envelopes, T, depend on the frequency and amplitude of excitation and for different parameters of excitation belonged to the interval $1/f_1 < T < 11/f_1$. Besides the excitation of modulated waves due to the interaction with basic harmonic frequency we found regimes with very low frequency modulation. The period of modulation was 10^2 times more than the period of the basic mode, T_1. Such regimes are shown in Fig. 3(c). It is worth mentioning that in this regime some slow modulation appears on the background of the modulation presented in Fig. 3(b); which is so-called an envelop modulation. We could not succeed in understanding whether the period of such low frequency modulation is multiple to the period of the first modulation. It is probably due to the finite time of observations: only several periods of low modulation were recoded in our experiments. During this time the long modulation seems to be regular.

Besides regular regimes, irregular modulation regimes have been found in the system. Typical time series of the regime with chaotic modulations are presented in Fig. 3(d). It should be emphasized that the occurrence of such regimes was not caused by the formation of surface waves of limited amplitude and wave breaking. It was revealed that the irregular motion arose when wave breaking was completely absent and surface waves had practically homogeneous structure in the direction perpendicular to the flume axis. For large amplitude of excitation wave breaking took place and the time series of free surface displacement demonstrate irregular behavior (see Fig. 3(e)).

To characterize the degree of regularity of surface displacement, correlation functions were calculated. These functions are presented in Fig. 4. For regular regimes of modulation the amplitude of correlation function does not practically decrease during ten period of the modulation (see Fig. 4(a), where period of mod-

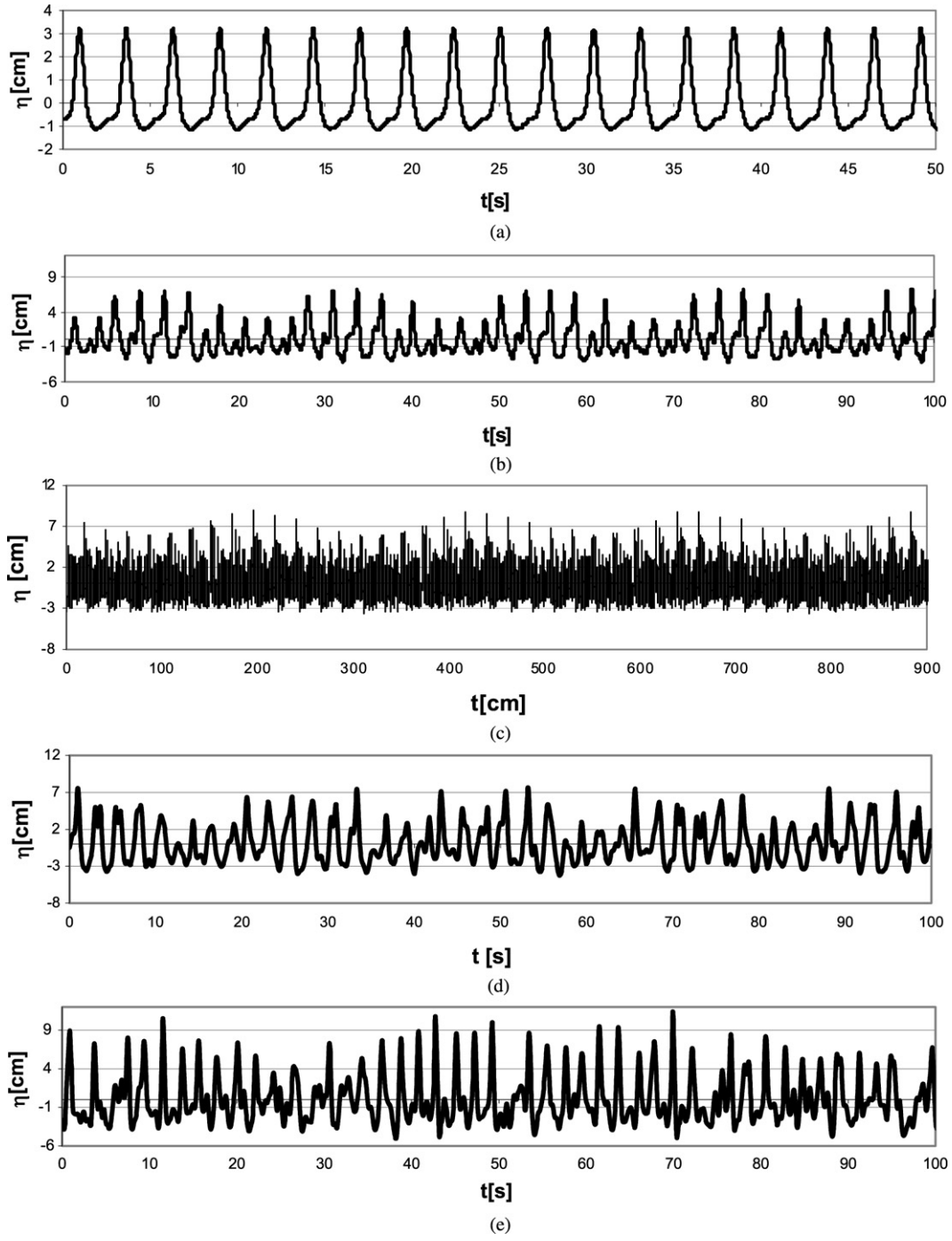

Fig. 3. Time series for different conditions of excitation: (a) the regime without modulation (amplitude $B = 45$ mm, $F = 0.3744$ Hz), (b) the regular modulation ($B = 48$ mm, $F = 0.3616$ Hz), (c) the double modulation ($B = 51$ mm, $F = 0.4058$ Hz), (d) the chaotic modulation without wave breaking ($B = 48$ mm, $F = 0.4$ Hz), and (e) the chaotic modulation due to wave breaking ($B = 48$ mm, $F = 0.4768$ Hz).

ulation T_{mod} is indicated). For the case of an irregular behavior without breaking, a weak decreasing of the correlation function amplitude (approximately 20%) was observed for the same time duration (see Fig. 4(b)). The correlation function for the wave breaking regime (Fig. 4(c)) differs fundamentally from regular and chaotic modulation cases. Fast decreasing (twice) of correlation function amplitude was observed at one period of waves excited in the flume. Such decay of correlation may be explained by the appearance of three-dimensional turbulent structures during the wave breaking. The surface displacement in such turbulent zones is not synchronized with the surface displacement of surface gravity waves; that leads to the decrease of the correlation function amplitude.

What is a modulated wave and how does it arise in the resonator? In order to answer this question we carefully investigated the transition from the regime of constant-amplitude wave generation to the regime with amplitude modulation. In the experiment we performed it as follows: when the regime of steady-state wave generation had been established in the system, we slightly changed the wavemaker frequency (by about 1–2%) and studied the transition to the regime with modulation. An example of such transition is given in Fig. 5.

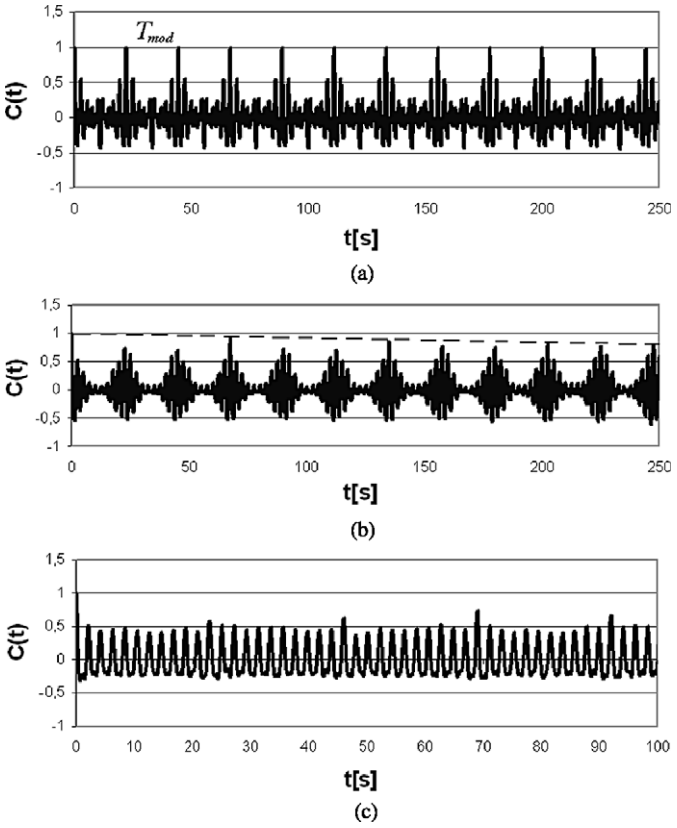

Fig. 4. Correlation functions $C(t)$ for time series: (a) the regime with regular modulation, (b) the regime with irregular modulation (dash line indicates decreasing of correlation function amplitude), (c) irregular modulation due to the wave breaking.

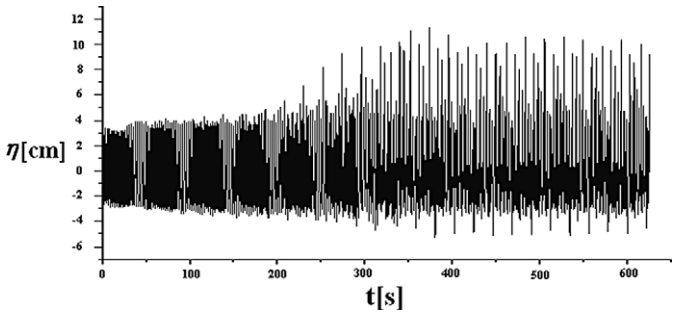

Fig. 5. Arising and growth of the modulation at the free surface corresponding to frequency change from $f = 0.413$ Hz to $f = 0.406$ Hz.

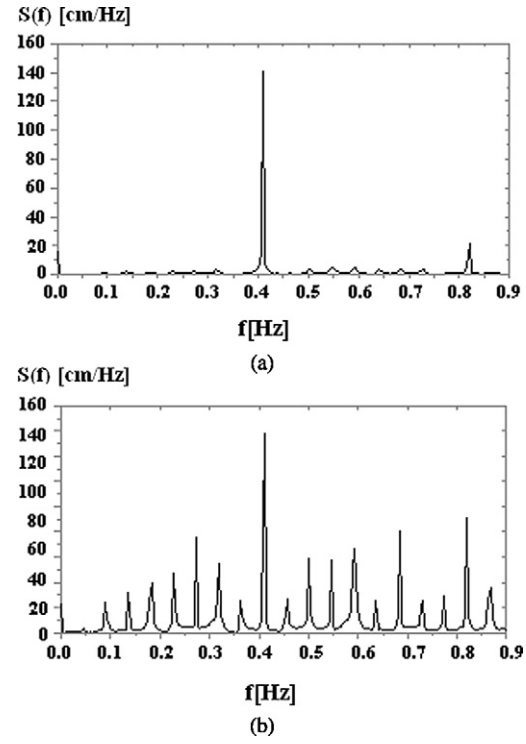

Fig. 6. Frequency spectra before (a) and after (b) the arising of the modulation shown in Fig. 5.

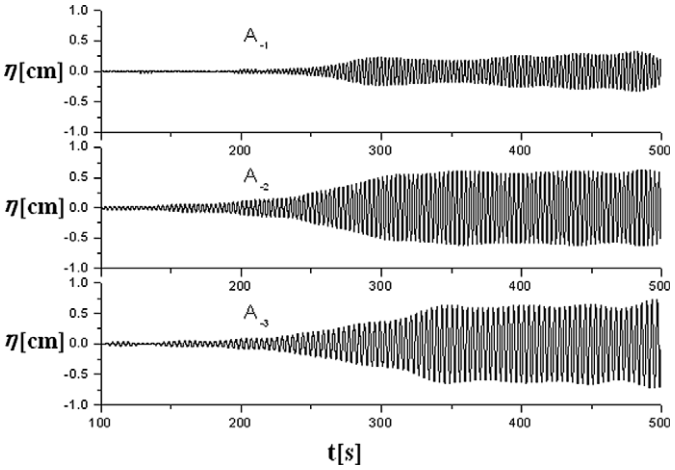

Fig. 7. Examples of band pass filtering of the time series in Fig. 5.

Fig. 6 represents a Fourier analysis of the time series before arising of the modulation ($0 < t < 200$ sec) and after the modulation growth (400 sec $< t <$ 650 sec). Fig. 6(b) shows clearly the presence of numerous harmonics excited in the resonator. The difference of frequencies Δf of the nearest spectral peaks in Fig. 6(b) is $\Delta f = 0.043$ Hz and is close to the frequency of the first resonator mode, f_1, obtained by using (2.1).

By using a narrow-band filtering it is possible to find how the amplitude of each satellite harmonic changes during the arising of modulation. For this purpose we used a band pass filtering (high and low cut-off frequency) whose bandwidth was set to half of $\Delta f = 0.043$ Hz. The examples of such filtering are presented in Fig. 7 for three harmonics. A similar temporal behavior was demonstrated by other harmonics: harmonics grow in amplitude from very small values, and when their amplitudes reach the order of magnitude of the fundamental harmonic amplitude, saturation takes place. It is possible to determine the temporal dependence of harmonic amplitudes for the interval of growth. The exponential function $A_n = A_n^0 \exp(\gamma_n t)$ gives us the best fit approximation for this time interval. Temporal dependence of the amplitude of satellite with $n = \pm 1, \pm 2, \pm 3$ is plotted in Fig. 8, the dependence of γ_n on satellite number n is presented in Fig. 9.

It is worth noting that the exponential growth rate is maximal for the satellites nearest to the fundamental mode, $n = \pm 1$ (see Fig. 9). This occurs when the amplitude of satellites is much less than the amplitude of fundamental harmonics. However, at the stage of saturation, when the amplitudes of harmonics are of the same order of magnitude as the amplitude of the fundamental harmonic, the amplitudes of distant satellites are maximal.

We can conclude that the occurrence of modulation is a result of instability of a nonlinear standing wave of finite amplitude. For the generation of the modulation some threshold of the amplitude of a nonlinear standing wave must be exceeded. The initial stage of the spectral sidebands growth from the noise level is exponential, and the nearest sidebands are initially most quickly growing. At

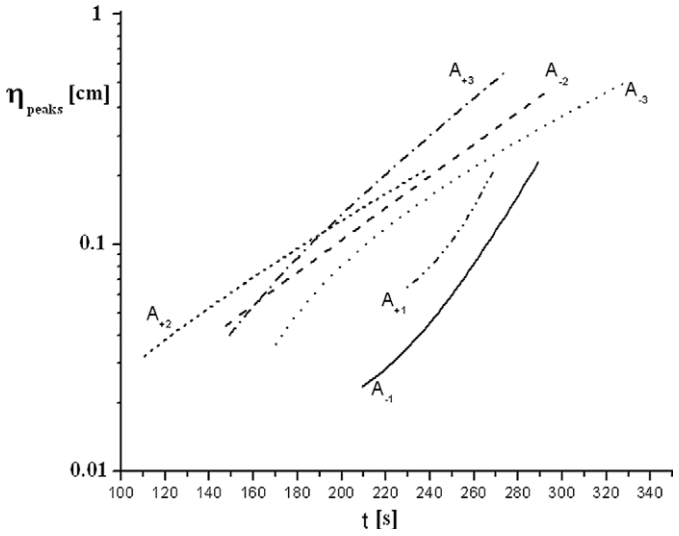

Fig. 8. Evolution of amplitudes during the modulation growth (satellites A_{-3} to A_{+3}).

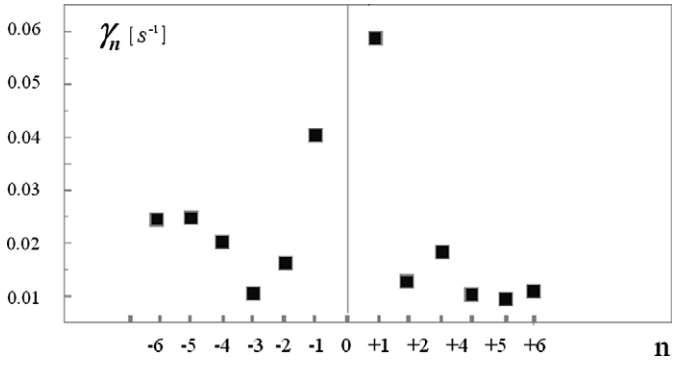

Fig. 9. Dependence of the exponential growth rate on the satellite number.

first sight it reminds the development of modulation instability but as we will show below, the physical mechanism of the modulated wave occurrence differs from that.

4. Numerical simulation of a resonator with forcing

This section is aimed at reproducing the regimes, observed during the laboratory experiment, in numerical simulations. To simulate the wave dynamics within a numerical tank, the primitive equations of ideal fluid, the potential Euler equations have been used. They are solved with the help of the High-Order Spectral Method, HOSM, following [12,13]. Since in the laboratory experiment transverse effects were noticeable only when waves broke, transverse dynamics is not taken into account in this study.

The kinematic and dynamic boundary conditions on the free surface are written in form

$$\frac{\partial \eta}{\partial t} = -\frac{\partial \Phi}{\partial x}\frac{\partial \eta}{\partial x} + \left(1 + \left(\frac{\partial \eta}{\partial x}\right)^2\right)\frac{\partial \varphi}{\partial z},$$
$$\frac{\partial \Phi}{\partial t} = -\eta - \frac{1}{2}\left(\frac{\partial \Phi}{\partial x}\right)^2 + \frac{1}{2}\left(\frac{\partial \varphi}{\partial z}\right)^2\left[1 + \left(\frac{\partial \eta}{\partial x}\right)^2\right] - P_a, \qquad (4.1)$$

where x and z are horizontal and vertical (upward) coordinates respectively, and t is time. Conditions $z = -h$ and $z = \eta(x,t)$ specify the water bed and the free surface displacement correspondingly. Function $\varphi(x,z,t)$ defines the velocity potential, and the potential at the surface is given by $\Phi = \varphi(x, z = \eta(x,t), t)$. Term P_a in (4.1) denotes the atmosphere pressure over the surface. Finally, the vertical component of the fluid velocity at the bottom, $z = -h$, is put equal to zero.

The velocity potential φ may be obtained after the iterative procedure for any prescribed functions $\eta(x,t)$ and $\Phi(x,t)$, when it is presented in the form of Taylor series about $z = 0$, see [12,13]:

$$\Phi(x,t) = \sum_{m=1}^{M}\sum_{k=0}^{M-m}\frac{\eta^k}{k!}\frac{\partial^k}{\partial z^k}\varphi_m(x, z=0, t),$$
$$\varphi(x,z,t) = \sum_{m=1}^{M}\varphi_m(x,z,t). \qquad (4.2)$$

In (4.2) the surface displacement $\eta(x,t)$ is small compared with wave length of disturbances, and number M defines the accuracy of the representation; in our simulations $M = 6$, which is often supposed to be a practically fully-nonlinear approach.

The application of spectral methods needs a computational domain with periodic boundary conditions. The rigid boundary in the tank provides the mirror-symmetry condition for the surface elevation and velocity potential. As it is observed in the laboratory experiment, a similar condition describes well the area near the wavemaker. Therefore, a 30-meter computational domain with the periodic boundary conditions was used in the numerical simulations of the 15-meter resonator. It is supposed, that $x = 0$ corresponds to the rigid wall of the laboratory resonator (where the gauge is situated, see Fig. 1), while $x = 15$ m corresponds to the other wall (position of the wave maker). In the most simulations the discretization mesh contains 1024 points, the integration in time is performed with the Runge–Kutta-4 method, and time step is 0.02 sec.

The HOSM is not originally designed for the introducing of a wavemaker. However, it admits variable in time and space pressure at the water surface, P_a, see (4.1), which we use as a virtual wavemaker with the purpose of exciting waves. It is defined by localized periodic pressure fluctuations in following form

$$P_a = P_0 \sin(2\pi f t)\exp\left(-\left(\frac{x - x_{wm}}{l_{wm}}\right)^2\right)\left(1 - \exp\left(-\frac{t}{t_{wm}}\right)\right). \qquad (4.3)$$

Here P_0 is the pressure amplitude, f is the excitation frequency, $x_{wm} = 15$ m is the position of the wave maker, l_{wm} is its characteristic size, and $t_{wm} = 20$ sec provides a smooth start of the excitation.

During the preliminary simulations it was found that the wave regimes (behavior of the wave record at the wall, $x = 0$, and the picture of the Fourier spectra) looked rather different from the ones observed in the laboratory experiment. While the laboratory experiments showed regular wave patterns, as Fig. 3(b), (c), the dynamics was irregular in the numerical simulations. Then, damping effects were introduced, adding extra terms on the right-hand sides of Eqs. (4.1) in the following way:

$$\frac{\partial \eta}{\partial t} = RHS - \mu\eta, \qquad \frac{\partial \Phi}{\partial t} = RHS - \mu\Phi. \qquad (4.4)$$

At first, parameter μ was taken constant, but then it was selected dependent on the wave scale, as

$$\mu = \delta k^2, \qquad (4.5)$$

where δ is a new constant, and k is the wave number. This choice provided pictures of the frequency spectrum, when modulations arise, qualitatively similar to the laboratory results.

The experiment described in Figs. 5, 6 was used as a test. Parameters P_0, and δ were tuned to be close to the laboratory conditions (characteristic wave amplitudes at the initial and modulational regimes, spectral pictures) in a better way. Thus, the damping parameter was fixed as $\delta = 0.0033$ sec^{-1}. Some dissipation was clearly observed in the laboratory tank; therefore the

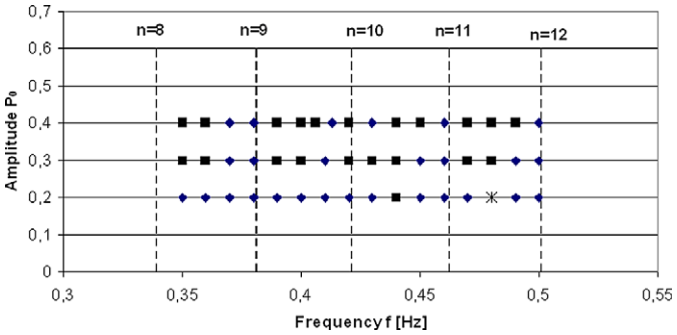

Fig. 10. The diagram of the regimes observed in the numerical simulations: rhombs correspond to the regimes of generation of constant-amplitude waves; squares – to regimes with modulated waves, star corresponds to the regime of double modulation; the dashed lines correspond to the frequencies of the natural modes with the numbers indicated in the figure.

introduction of damping into the numerical scheme seems to be reasonable, although a quantitative estimation of the wave dissipation in the laboratory experiment is not evident. The frequency-dependent damping (4.5) corresponds to the viscous effects law k^2 following from the Navier–Stokes equation, and thus is also natural.

The direct relation between the paddle amplitude, B, and the pressure amplitude, P_0 is not straightforward; therefore different values of P_0 were used to perform sets of numerical simulations for different values of the excitation frequency, f, in the interval $0.35\ \text{Hz} \leqslant f \leqslant 0.5\ \text{Hz}$. These results are summarized to obtain a diagram in Fig. 10 similar to the one in Fig. 2 for the laboratory observations. Breaking or even very steep waves cannot be simulated with the help of the HOSM, which limits the maximum value of the parameter P_0. On the other hand, damping (4.4)–(4.5) plays the role of a high-frequency filter, which improves the stability of simulations.

The diagram in Fig. 10 shows the regions when modulated and non-modulated waves in the time series are retrieved at the wall ($x = 0$). It qualitatively agrees with Fig. 2, although the forcing strength is characterized in Fig. 2 by the wavemaker amplitude, and in Fig. 10 – by the pressure amplitude. Different regimes observed in the laboratory experiments are found in the numerical simulations as well. Dynamics with modulation is observed when the forcing pressure has large values, while weak excitation leads to regular waves. Resonance structure in the diagram is clearly seen, i.e., modulations occur only in some regions of the plane; they correspond to the resonator modes. It should be stressed that the determining of the regime type (modulations or regular waves) is not unambiguous, since sometimes modulations grow very slowly. The double-periodic modulation was found once on the diagram in Fig. 10 (see the star symbol). The regime with no modulations is presented by Fig. 11(a). Fig. 11(b) exhibits the regime when modulations arise, and Fig. 11(c) illustrates case when double modulation is observed. On the spatio-temporal diagram in Fig. 11(b) the traveling intense wave patterns are clearly seen, in contrast to Fig. 11(a), where the wave field picture is uniform. Some wave shape asymmetry may be also observed due to the dissipation effect. The parameters of excitation P_0 and f are given in the figure captions. Fig. 11(a)–(c) qualitatively correspond to Fig. 3(a)–(c).

The development of wave modulations may happen quickly or very slowly, if the excitation frequency is chosen between the one, responsible for regular waves, and the second, resulting in rapid occurrence of modulations. The regime with double modulation in Fig. 11(c) is found for the excitation frequency value $f = 0.48$ Hz, although this effect here is less pronouncing than the one shown in Fig. 3(c). Mode 11 is the most energetic in the case presented in

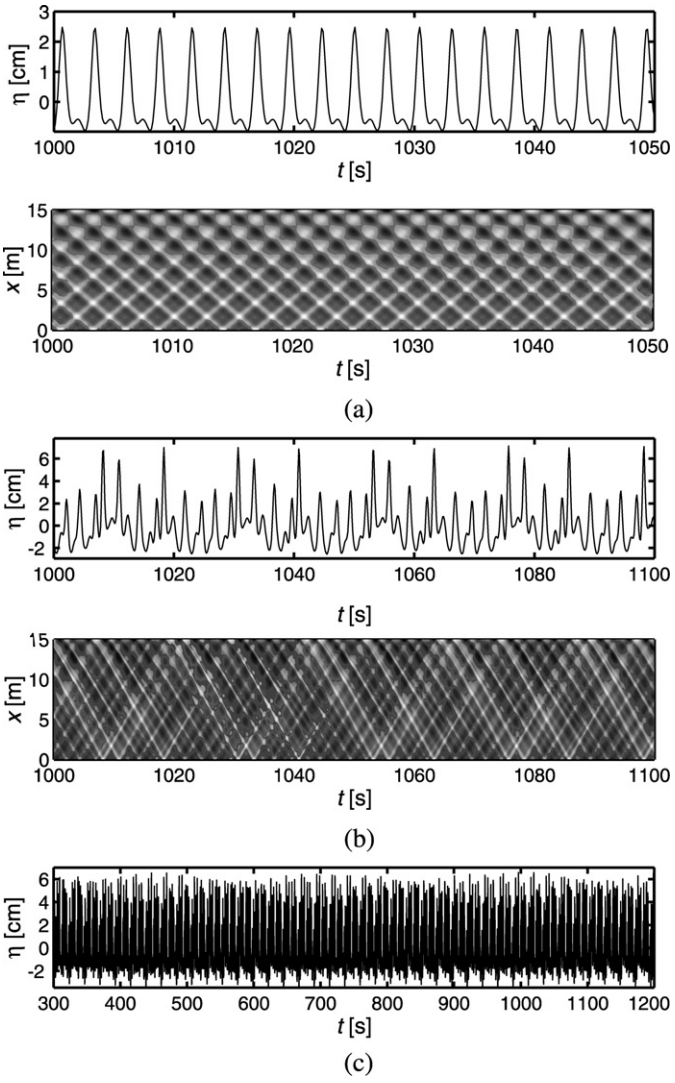

Fig. 11. Wave dynamics observed in the numerical simulations (the time series of the surface displacement retrieved at the wall versus time): (a) regular non-modulated waves ($P_0 = 0.2$ Pa and $f = 0.37$ Hz): the time series and the spatio-temporal diagram, (b) wave dynamics with modulations arise ($P_0 = 0.3$ Pa and $f = 0.40$ Hz): the time series and the spatio-temporal diagram, (c) double modulations ($P_0 = 0.3$ Pa and $f = 0.48$ Hz): the time series.

Fig. 11(c); the long-term oscillations (the modulation of the envelope) have a duration of about 250 s, while the period of the first resonator mode is about 23 s.

The frequency spectra (hereafter the spectrum is defined as the amplitude of the Fourier transform in time or in space) computed from the time-series in Fig. 11(a), (c), are given in Fig. 12. It is seen that a standing wave is represented by the main spectral peak at the excitation frequency, and also by some bound harmonics due to nonlinearity (Fig. 12(a)). Strongly modulated waves correspond to many excited frequencies, as it is shown in Fig. 12(b) for the regime with double modulation (see Fig. 11(c)); the spectrum for the case shown in Fig. 11(b) is qualitatively similar, although for different parameters of excitation the energy exchange between many excited spectral harmonics (as in Fig. 12(b)) may vary a lot.

In Fig. 12(b) dotted vertical ticks show the linear natural resonator frequencies, and the frequencies f_1, f_{11}, f_{16}, f_{22} and f_{33} are labeled; the frequency of the excitation, f, is shown by a solid vertical line. It is well-seen that low-frequency peaks correspond to the natural resonator frequencies rather well, while higher frequencies shift to the right. This leads to the intersection of reso-

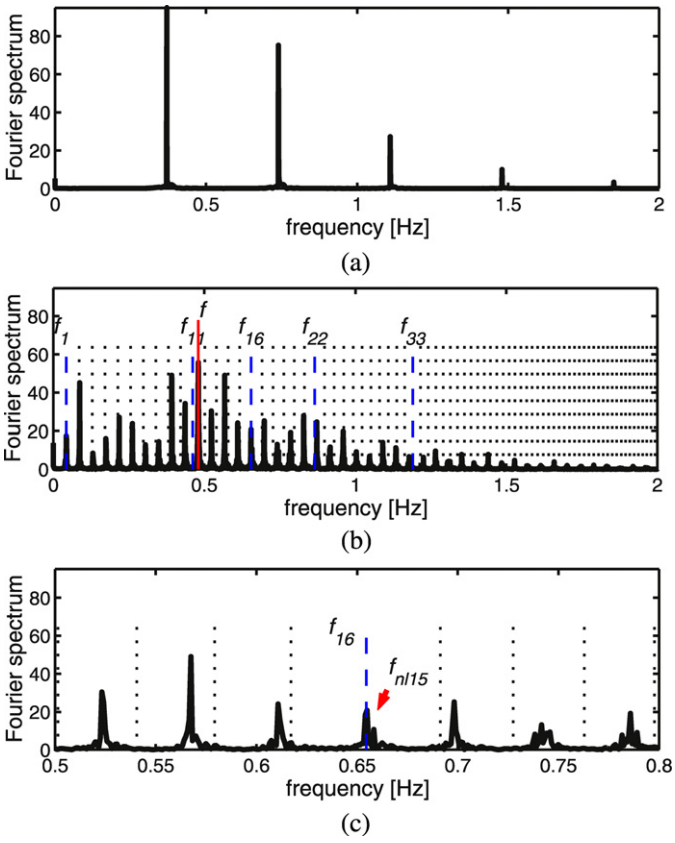

Fig. 12. Frequency Fourier spectra of the time series given in Figs. 11(a) and 11(c). Parameters of the excitation: (a) $P_0 = 0.3$ Pa and $f = 0.37$ Hz; (b) $P_0 = 0.3$ Pa and $f = 0.48$ Hz; (c) enhanced part of spectrum from panel (b) around frequency f_{16}. See the text for the explanation of panels (b), (c).

nance frequencies, so that the linear frequency of mode 16, f_{16}, is very close to a nonlinear resonance spectral peak of mode 15, see Fig. 12(b). As a result, this frequency peak is doubled, representing the linear frequency mode 16 (peak f_{16}), and essentially nonlinear mode 15 (shown by an arrow in Fig. 12(c), which is extended from Fig. 12(b)). This effect may be supposed to be an explanation of the double modulation (the slow modulation of the envelope).

5. Numerical simulation of the free evolution of perturbed standing waves

Although a qualitative agreement between laboratory experiments and numerical simulations is achieved in Section 4, the physical understanding of the phenomenon why and how modulations develop in the resonator is difficult, since the dynamics is complicated being represented by many excited resonator modes. Let us now consider in this section a simpler problem of a free wave evolution in the resonator. Eqs. (4.1)–(4.2) govern this dynamics, with no damping or excitation ($\delta \equiv 0$, $P_a \equiv 0$).

5.1. Excitation of standing waves

The standing-type waves excited in the laboratory tank obviously differ from the exact standing water-wave solution for the Euler equation due to the following reasons: (i) the piston-type wavemaker produces a complicated water movement nearby; (ii) the wave damping during the wave propagation is readily observed. Therefore the initial condition in a form of a standing wave was produced in a rather rough way as follows. The zero initial conditions are used, $\eta(x, t = 0) = 0$, $\varphi(x, z, t = 0) = 0$; at time $t = 0$

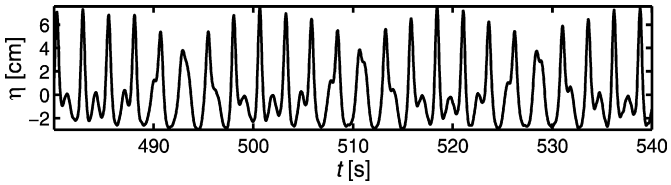

Fig. 13. Example of the evolution of excited standing waves. The time series of the surface displacement retrieved at the wall versus time.

a periodic pressure fluctuations start oscillating with constant frequency, f,

$$P_a = 0.03 \sin(2\pi f t) \cos(2\pi n x). \tag{5.1}$$

Here n is the resonator mode number. The frequency f is not equal to the linear resonator mode frequency f_n (2.1), due to the nonlinear corrections. It was corrected as

$$f = f_n / c_{fr}, \tag{5.2}$$

where constant c_{fr} is determined by the selection to make the wave excitation more efficient. Value $c_{fr} = 1.034$ provided the generation of almost breaking waves during several oscillations for most considered cases. Breaking waves cannot be simulated with the help of the HOSM, when waves become too steep, the numerical simulation becomes unstable.

This approach was applied to produce initial conditions in the form of nonlinear standing waves corresponding to different modes of the resonator, n. Fig. 13 shows the free evolution of such a wave, excited with $n = 9$. The surface displacement in the numerical tank reaches values of about 7.5 cm. The wave system exhibits close to periodic evolution for rather a long time. Some beating effect resulting in wave patterns formation is readily seen in Fig. 13. It is due to the fact that the standing wave is actually represented by several modes excited by the variable pressure (5.1). On the corresponding frequency Fourier spectrum the main spectral peak at frequency 0.4 Hz (corresponding to the mode 9 of nonlinear standing wave) and smaller peaks near the double frequency (corresponding to the bound wave of the nonlinear mode 9, and also to the free counter-propagating waves of mode 18) may be distinguished. The latter two frequency peaks are of similar magnitudes. Analyzing the spatial spectrum, we conclude that multiple modes $n = 9, 18, 27$ contain the bigger part of energy, while other modes keep very little energy. Some energy exchange between excited free standing modes makes the wave dynamics more complicated than classical linear beating effect.

Thus, the excited standing wave is not a pure 9-mode wave, but includes some standing waves of multiple modes. We should note that more accurate methods to generate standing waves of a certain mode do exist (for example, [14]). However, the employed approach seems to be sufficient for our purposes in the present study, since modes except the multiple ones are not excited.

5.2. Free evolution of perturbed standing waves

The modulational effects observed in the laboratory experiments looked very similar to the Benjamin–Feir self-modulations. Therefore, stability of the wave system in the resonator with respect to sideband perturbations has been studied. For this purpose the excited, as it is described just above, standing wave, defined by fields $\eta(x, t = 0)$ and $\Phi(x, t = 0)$, was weakly modulated in the following way,

$$\eta_{\mathrm{mod}} = \eta(x, t = 0)\left(1 + \varepsilon \cos\left(\frac{\pi x}{L}\right)\right),$$
$$\Phi_{\mathrm{mod}} = \Phi(x, t = 0)\left(1 + \varepsilon \cos\left(\frac{\pi x}{L}\right)\right), \tag{5.3}$$

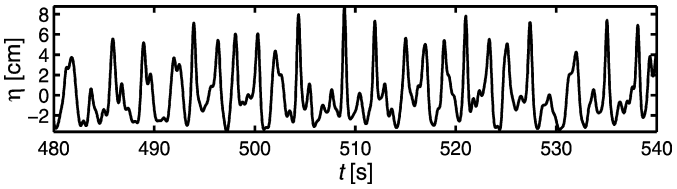

Fig. 14. The evolution of standing waves with excited sidebands. The time series of the surface displacement retrieved at the wall versus time.

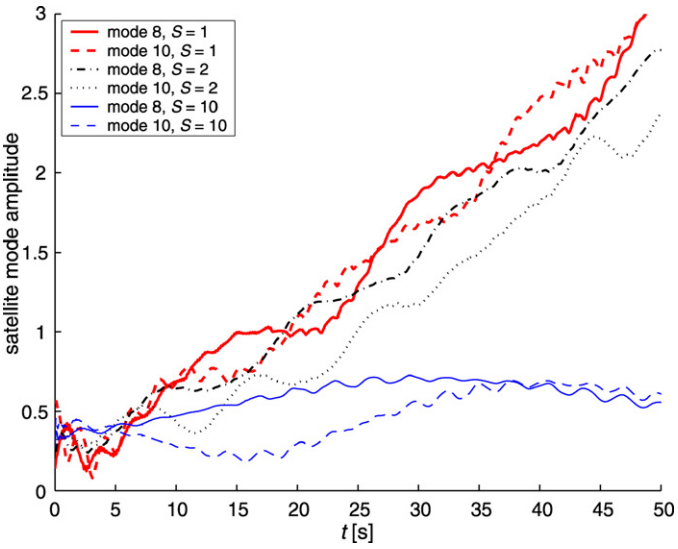

Fig. 15. Evolution of satellite mode amplitudes for scaled initial conditions η_S and Φ_S for $S = 1$, $S = 2$ and $S = 10$. The scaled vertical axis gives AS, and the scaled horizontal axis gives t/S. The tick labels correspond to the case $S = 1$.

where ε is a small parameter, and $L = 15$ m is the resonator length. The free evolution of the new initial condition was then computed with the HOSM. Modulation (5.3) results in the existence of small sideband satellites in the spatial spectrum of the waves. It is found that the satellites may grow in time, which leads to the growth of wave modulations. The satellites grow when parameter ε is large enough, and when the standing waves are sufficiently high.

The wave dynamics, when the modulations are developed, is presented in Fig. 14, which is similar to Fig. 13, but now the standing wave is perturbed at $t = 0$ following (5.3) with $\varepsilon = 0.05$, which leads to the presence of some little inoculating energy in modes 8 and 10. The initial stage of the evolution of mode 8 and 10 amplitudes is given in Fig. 15 (thick solid and dashed lines). While the satellites grow, the mode 9 loses energy. The energy from mode 9 leaks first to the sidebands, and then many modes become energetic, so that the wave dynamics becomes very irregular, see Fig. 14. The corresponding frequency spectrum also becomes complicated and shows many energetic peaks similar to Fig. 12(b).

Aiming at revealing the main nonlinear wave interaction responsible for the growth of the sidebands, the initial conditions (5.3) that were used to start simulations shown in Fig. 14 were scaled as

$$\eta_S = \eta_{\mathrm{mod}}/S, \quad \text{and} \quad \Phi_S = \Phi_{\mathrm{mod}}/S. \tag{5.4}$$

Parameter S plays the role of a scaling factor; value $S = 1$ corresponds to the already considered case (5.3).

The evolution of satellite mode amplitudes, A, at initial stage of the growth is given in Fig. 15 for values $S = 1$ (as it has been described just above), and also for $S = 2$ and $S = 10$. The curves in Fig. 15 are plotted in scaled axes, AS and t/S. One may conclude that in the scaled axes the curves for cases $S = 1$ and $S = 2$ are qualitatively similar. This scaling corresponds to a process with quadratic nonlinearity, i.e., three-wave interactions are responsible for the satellite excitation. This conclusion is, however, limited by some ranges of wave amplitudes, since for larger S (smaller standing waves) this qualitative relation breaks, so that in case $S = 10$ there is no significant growth of the sidebands at all, even for longer times (see thin solid and dashed lines in Fig. 15). The perturbation does not grow either, when the perturbation is not sufficient (for example, the considered standing wave remain stable when $\varepsilon = 0.01$ in (5.3)).

6. Spatio-temporal spectrum in numerical simulations

To briefly conclude, the development of strong wave modulations is observed for some frequencies and for sufficiently high waves. The conditions of experiments do not satisfy the classical modulational (four-wave) instability criterion for unidirectional free waves over finite depth, since for the considered modes $kh < 1.363$. Moreover, the process is mainly caused by three-wave interaction as shown in Section 5. Exact three-wave resonances do not exist for gravity water waves; although near-resonance conditions due to nonlinearity may in principle occur for sufficiently shallow water and intense waves.

The strength of nonlinear effects due to 3-wave interactions over shallow water may be estimated with the help of the Ursell parameter

$$Ur = \frac{a\lambda^2}{h^3} \propto \frac{ak}{(kh)^3}, \tag{6.1}$$

where a is the wave amplitude, and λ is the characteristic wavelength (see for instance [15]). The Ursell number, Ur, should be small if approximate weakly nonlinear equations for weak perturbations (of nonlinear Schrödinger equation, NLS type) are concerned. For a Korteweg–de Vries soliton, its value is $Ur = 4$, which defines the quantitative measure of the strength of nonlinear effects. It may be straightforwardly estimated that the Ursell number is nevertheless large for the conditions of our laboratory experiments. The shallower water, the smaller waves should be in order to fulfill the condition of a small Ursell number. Actually, for the mode 9 of our resonator request $Ur \ll 4$ leads to the restriction $a \ll 1$ cm. Therefore, the considered waves cannot be supposed as quasi-sinusoidal, but are essentially cnoidal waves, and a NLS-like approach cannot be successful.

It was already pointed out that the registered frequencies of resonator modes are higher than compared with the linear case. Thus, the nonlinear corrections lead to a frequency increase for long waves. The laboratory data contains limited information since it is represented only by time-series measured at one point. Interpretation of the frequency spectra may be rather sophisticated as demonstrated in Section 4. To improve the understanding of the phenomenon the advantage of having the full information about the waves in numerical experiments is employed. The spatio-temporal spectra of waves are computed and are discussed in this section.

The diagrams of spatio-temporal spectra are obtained as follows. First, the spatial Fourier transform of the surface elevation as function of space and time is performed. Then the temporal Fourier transform is applied to the modes of the spatial Fourier spectrum, represented by complex data time series. Thus, spatio-temporal spectra $Sp(n, f)$ are obtained, where n is the mode number, and f is frequency. The length of a time series defines the frequency resolution, which is not less than 0.005 Hz for the presented figures. To render the intensity of the Fourier spectrum, Sp, every value of it (for the grid in the plane of modes and frequen-

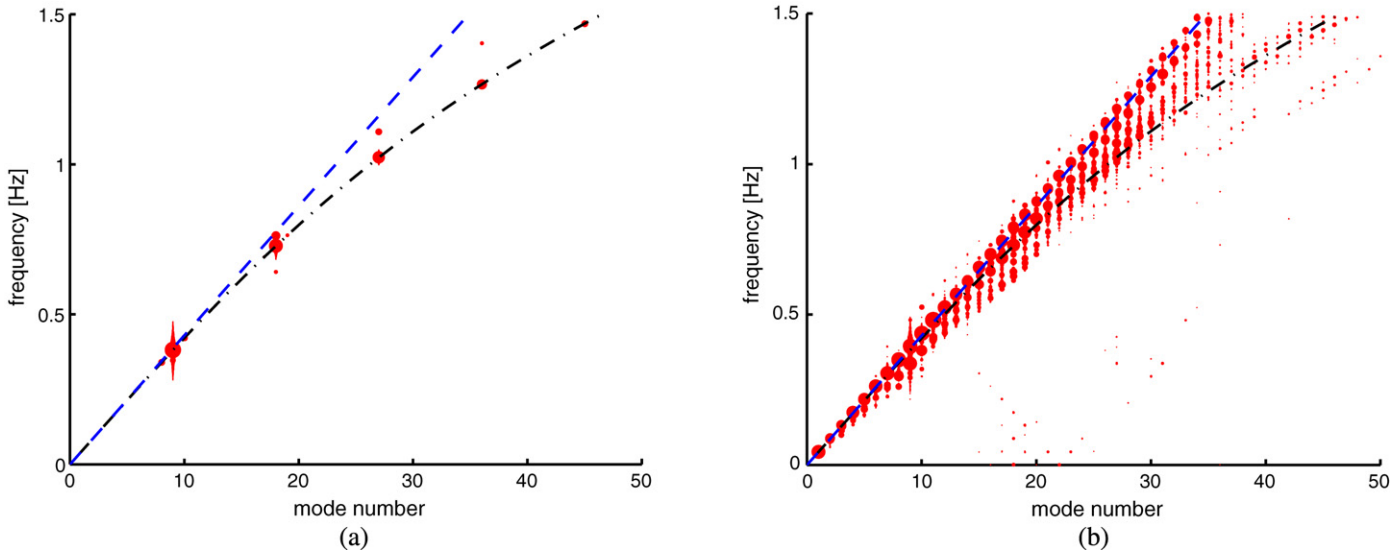

Fig. 16. Spatio-temporal spectral plane for the numerical experiments of scaled perturbed standing wave free conservative evolution (see Fig. 15 and description to it). (a) case $S = 10$ (small amplitude), (b) case $S = 1$ (large amplitude, growth of modulations). The dash-dotted lines represent the exact linear dispersion, its shallow-water limit is given by the dashed straight lines.

cies) is plotted by a filled circle with diameter, D, proportional to the amplitude of Sp in logarithmic scale, more precisely,

$$D = 1 + \frac{1}{5} \ln \frac{|Sp|}{\max_{n,f} |Sp|}. \tag{6.2}$$

Only positive values of D are considered, which neglects too small (insignificant) values of Sp.

Let us first consider free conservative evolution of weakly perturbed standing waves of different amplitudes described in Section 5. Fig. 16 gives the spatio-temporal spectra corresponding to the cases shown in Fig. 15 for $S = 10$ (Fig. 16(a), no modulation) and $S = 1$ (Fig. 16(b), modulations arise). The dash-dotted lines in Fig. 16 represent the exact linear dispersion (2.1), the shallow-water limit is given by the dashed straight lines.

Fig. 16(a) illustrates the case of small-amplitude waves, when modulations do not grow. Energy corresponding to small-amplitude free waves is located on the dispersive curve; the energy is represented by large circles lying on the dash-dotted curve in Fig. 16(a). Nonlinear bound waves are represented by smaller circles (less energetic spots) in Fig. 16(a) aligned higher than the dispersive curve, but lower than the shallow-water dispersion limit (the dashed line). The most energetic mode is number 9. If we denote its mean frequency as f, then the bound modes are situated on the spectral plane at $(9m, mf)$, where m is an integer. Some small-energetic spots due to nonlinear interactions may be found in Fig. 16(a), and they are much more in Fig. 16(b).

The diagram in Fig. 16(b) represents the regime with modulations, and is quite different and complicated. There are many energetic spots; the energy is spread along the curve of the shallow-water dispersion limit, and less – along the linear dispersion curve. For a given mode number the frequency spectrum is rather wide.

The forced experiments described in Section 4 are described below. Spatio-temporal spectra for the regimes presented in Fig. 11(a), (b) are given in Figs. 17 and 18 respectively. The horizontal dotted lines in the Figs. 17, 18 show the forcing frequencies, f, and also multiple values $2f$, $3f$, etc. Similar to Fig. 16, the dash-dotted lines represent the exact linear dispersion (2.1), its shallow-water limit is given by the dashed straight lines. The solid straight lines in Figs. 17, 18 are lined through the reference origin $(0, 0)$, and the point (n, f), where n is the most excited mode at the forcing frequency f ($n = 9$ for Figs. 17, 18). Thus, this line

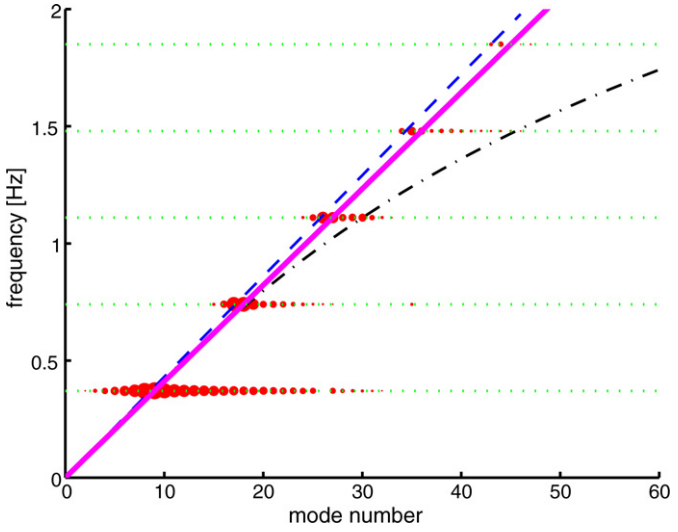

Fig. 17. Spatio-temporal spectral plane for the numerical experiment with excitation $P_0 = 0.3$ Pa and $f = 0.37$ Hz (see Fig. 11(a)). The dash-dotted lines represent the exact linear dispersion, its shallow-water limit is given by the dashed straight lines. The horizontal dotted lines show the frequency and multiple frequencies of the excitation.

on the spectral plane represents the phase velocity of the most excited standing wave.

Fig. 17 corresponds to the regime when modulations do not occur (see Fig. 11(a)). Fig. 18(a) corresponds to the case when the modulations have not arisen, but will develop later (the early stage of the regime shown in Fig. 11(b)). Fig. 18(b) shows the case of developed modulations (see Fig. 11(b)). The spots in Figs. 17 and 18(b) are discrete in both mode and frequency. The frequency discretization is due to the regular character of the record, and its interval is larger than the resolution. In Figs. 16 and 18(a) the frequency does not seem to be sampled due to irregular character of the waves. One driving frequency excites many modes, as it is seen in Figs. 17, 18; this is in part due to significant size of the forcing region, l_{wm}. Bound modes are also excited; the most energetic part of them lies on the solid magenta line, which represents waves with the same phase velocity as the most excited mode component on the forcing frequency. Therefore we will refer this line to as the *forcing wave velocity*.

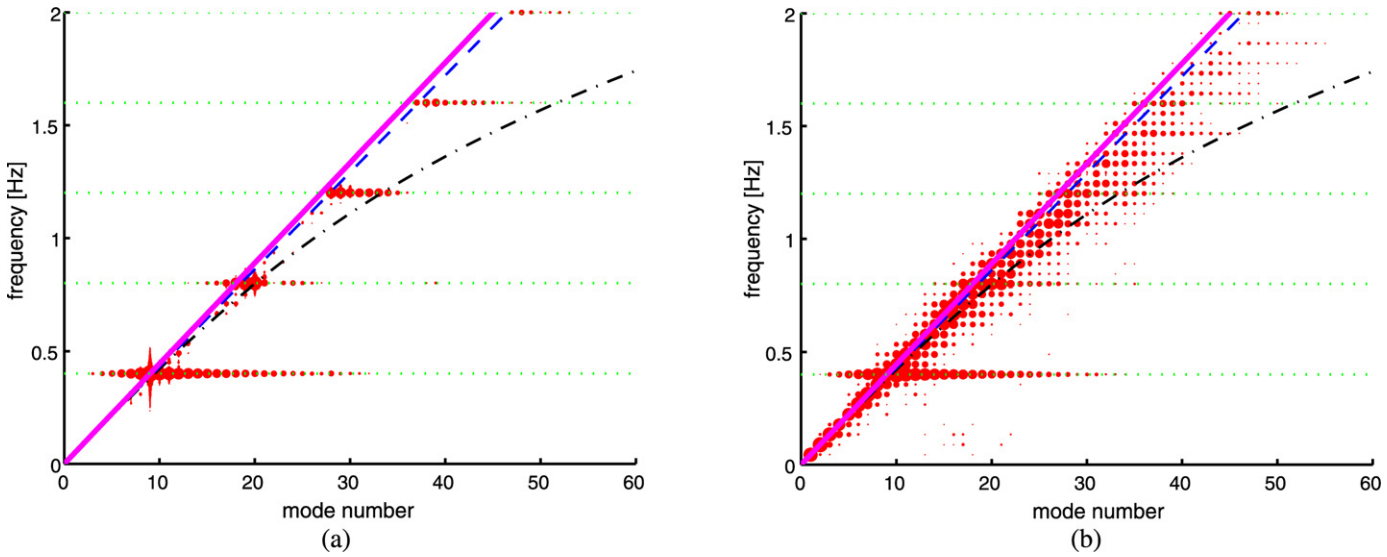

Fig. 18. Spatio-temporal spectral plane for the numerical experiment with excitation $P_0 = 0.3$ Pa and $f = 0.40$ Hz (see Fig. 11(b)): (a) before the modulations become developed ($0 < t < 200$ sec), (b) for developed modulation (300 sec $< t < 1200$ sec). The dash-dotted lines represent the exact linear dispersion, its shallow-water limit is given by the dashed straight lines. The horizontal dotted lines show the frequency and multiple frequencies of the excitation.

When the forcing wave velocity is equal to the phase speed of other waves, the 3-wave resonance condition becomes fulfilled. It is known, that in a 3-oscillator system with quadratic nonlinearity, lower frequencies may effectively get energy from the high-frequency oscillator (this process is exponential at its early stage, see [16]). Due to the nonlinear frequency correction, and the case of intense waves, the condition when the 3-wave resonance occurs is not evident. However, it clearly follows from Figs. 17 and 18, that modulations do not grow when the forcing wave velocity curve is lower than the shallow-water limit of the dispersion (Fig. 17). In the opposite, the modulations grow when the forcing wave velocity is higher than the long-wave speed (Fig. 18). It may be concluded that the 3-wave resonance condition with the driving wave becomes fulfilled due to positive nonlinear frequency shift to a number of low modes, and then the modulations arise. This dynamics involves many wave triplets, thus may be hard to interpret. Besides free waves, many bound waves are excited, since the waves are essentially cnoidal.

It may be found from Fig. 18(a), that at the initial stage of modulation growth just few modes and frequencies are excited close to the most forced wave. When the modulations are developed, the line of forcing wave velocity has frequency spectral peaks at every mode until at least four times the most excited mode number, see Fig. 18(b), which confirms that this line represents the resonance condition. Note that the condition for Benjamin–Feir instability $kh > 1.363$ becomes fulfilled for modes $n > 38$. Besides free waves, many bound waves are excited, since the waves are essentially cnoidal; many other modes and frequencies hold energy due to nonlinear interactions.

7. Discussion

Different wave regimes were observed in a shallow water resonator with periodic wave excitation at the wall: (1) steady-state nonlinear waves with constant amplitude, (2) regular and chaotic wave modulations without breaking, including double modulations; and (3) regime with modulation accompanied by wave breaking. In the present study, we focus our interest on the regimes when the modulations arise, and are not accompanied by breaking. It was found in the laboratory experiments that this effect occurs for sufficiently high waves (large amplitudes of the wavemaker) and for frequencies apart from the natural resonator frequencies, see Fig. 2. The laboratory experiments report about exponential growth of frequency sidebands when modulations arise.

All the regimes observed in the laboratory experiment, not accompanied by wave breaking, are reproduced qualitatively by means of strongly-nonlinear numerical simulations. Wave damping was found necessary for the achievement of regimes with regular wave modulations. The dynamics is also sensitive for the damping law. The forcing was introduced to the numerical scheme through surface pressure variations. Similar to the laboratory experiments, the regimes when modulations arise for certain strengths and frequencies of excitation are found. Thus, weakly nonlinear waves do not suffer from the unstable modulational growth discussed in this paper. It is found that intense standing waves become modulated when weak long modulations are introduced. The initial stage of this effect is proved to be governed by 3-wave interactions; and also amplitude threshold exists for the minimum wave amplitude, when the perturbations grow.

Though shallow-water conditions are fulfilled ($kh < 0.42$ for the main excited modes), the wave amplitudes are too large, so that the Ursell number is not small, thus the waves are essentially cnoidal, and approximate models for weak modulations of quasi-sinusoidal waves are not applicable.

On the basis of numerical simulations of the strongly-nonlinear pseudo-spectral constant-depth model it is found that the 3-wave resonance conditions become fulfilled due to the positive frequency nonlinear shift. When the excited counter-propagating waves have phase velocity larger than the linear long-wave speed, these waves enter in resonance with long-wave perturbations. Thus the latter effectively get energy driven by the wavemaker waves. In the simplified model of three coupled weakly nonlinear oscillators, this energy leakage is exponential and leads to a very strong exchange of energy between the oscillators. In our case, not only one triplet, but many low modes become in resonance with the driven wave, and thus they become excited. Nonlinear bound modes and combined frequencies and wavenumbers appear due to the interaction of excited modes. Finally, many modes on the spatio-temporal spectral planes are energetic, see Fig. 18(b). Only a part of them represents free waves with frequencies shifted upward due to nonlinearity, while other spots on the resonance line in Fig. 18(b) – are bound nonlinear modes.

The last paragraph may be formulated otherwise. It is shown in Section 5 that the nonlinear standing wave dynamics may support

growth of small long perturbations. Thus, when the excitation parameters, i.e., frequency and the excited standing wave amplitude, obey the relation for a nonlinear standing wave of some mode in this resonator, then weak perturbations grow, and modulations occur; they may be regular due to dissipation effects. When the excitation conditions are far from the nonlinear resonator natural mode parameters, only few harmonics in the frequency and wave number spectra exist, and modulations of standing waves do not develop.

The nonlinear wave dynamics in a shallow water resonator was investigated by means of the numerical solution of the Boussinesq system in [17]. Importance of three-wave interactions revealed in the present study may prove that simplified models (like Boussinesq of Korteweg–de Vries equations) could be able to describe the observed phenomena, and be helpful in obtaining quantitative estimates. This problem will be a topic for the further research.

Acknowledgements

The experimental tests were supported by a French national scientific program called 'PLAMAR'. The research was supported for AS by RFBR grants 06-05-72011, 08-02-00039 and grant of the leading Scientific School NSh-1244.2008.2.

References

[1] T.B. Benjamin, J.E. Feir, The disintegration of wave train on deep water. Part 1. Theory, J. Fluid Mech. 27 (1967) 417–430.
[2] V.E. Zakharov, Stability of periodic waves of finite amplitude on the surface of deep fluid, J. Appl. Mech. Tech. Phys. 2 (1968) 190–194.
[3] G.B. Whitham, Linear and Nonlinear Waves, Wiley-Interscience, New York, 1974.
[4] D.J. Benney, G.J. Roskes, Wave instabilities, Stud. Appl. Math. 48 (1969) 377–385.
[5] A. Davey, K. Stewartson, On the three-dimensional packets of surface waves, Proc. R. Soc. Lond. A 338 (1974) 101–110.
[6] J.W. McLean, Instability of finite-amplitude gravity wave on water of finite depth, J. Fluid Mech. 114 (1982) 331–341.
[7] M. Francius, C. Kharif, Three-dimensional instabilities of periodic gravity waves in shallow water, J. Fluid Mech. 561 (2006) 417–437.
[8] M. Onorato, A.R. Osborne, M. Serio, Modulational instability in crossing sea states: A possible mechanism for the formation of freak waves, Phys. Rev. Lett. 96 (2006), 014503-1–4.
[9] T.J. Bridges, F.E. Laine-Pearson, Nonlinear counter propagating waves, multisymplectic geometry, and the instability of standing waves, SIAM J. Appl. Math. 64 (2004) 2096–2120.
[10] S.N. Vlasov, V.I. Talanov, Wave Self-Focusing, Institute of Applied Physics Press, Nizhny Novgorod, 1997 (in Russian).
[11] S.D. Griffiths, R.H.J. Grimshaw, K.R. Khusnutdinova, Modulational instability of two pairs of counter-propagating waves and energy exchange in two-component media, Physica D 214 (2006) 1–24.
[12] D. Dommermuth, D.K.P. Yue, A high-order spectral method for the study of nonlinear gravity waves, J. Fluid Mech. 184 (1987) 267–288.
[13] B.J. West, K.A. Brueckner, R.S. Janda, D.M. Milder, R.L. Milton, A new numerical method for surface hydrodynamics, J. Geophys. Res. 92 (1987) 11803–11824.
[14] M. Okamura, Long time evolution of standing gravity waves in deep water, Wave Motion 23 (1996) 279–287.
[15] E. Pelinovsky, Hydrodynamics of tsunami waves, in: J. Grue, K. Trulsen (Eds.), Geophysical Fluids: Tsunamis, Rogue Waves, Internal Waves and Internal Tides, in: CISM Courses and Lectures, vol. 489, Springer, 2006, pp. 1–48.
[16] M.I. Rabinovich, D. I Trubetskov, Oscillations and Waves in Linear and Nonlinear Systems, Kluwer Academic Publisher, Dordrecht, 1989.
[17] A.B. Ezersky, O.E. Polukhina, J. Brossard, F. Marin, I. Mutabazi, Spatio-temporal properties of solitons excited on the surface of shallow water in a hydrodynamic resonator, Phys. Fluids 18 (2006) 067104.